Reversible Single-Crystal-to-Single-Crystal Transformations of Metal−Organic Frameworks that Accompany Two-Dimensional Framework Reorganizations

Published as part of a Crystal Growth and Design virtual special issue on Crystal Engineering of Nanoporous Materials for Gas Storage and Separation

Sunyoung Shin, Seok Jeong, Dongwook Kim, and Myoung Soo Lah*

Department of Chemistry, UNIST, Ulsan 44919, Korea

Ⓢ *Supporting Information*

ABSTRACT: A three-periodic (3-P) metal−organic framework (MOF) based on a one-periodic (1-P) *rhomboidal chain* as a supermolecular building block (SBB) can be transformed to another stable 3-P MOF by a postsynthetic exchange of ligands in a single-crystal-to-single-crystal (SCSC) fashion that accompanies the unprecedented two-dimensional (2-D) structural reorganization. The enhanced framework rigidity of the new MOF allows partial but systematic deletion of some organic linkers from the framework, which leads to the other 3-P MOF. The SCSC transformations can occur reversibly by postsynthetic exchange, deletion, and insertion of the ligands, while the stable 1-P SBB plays a pivotal role during the transformations that accompany significant 2-D reorganization of the framework structures.
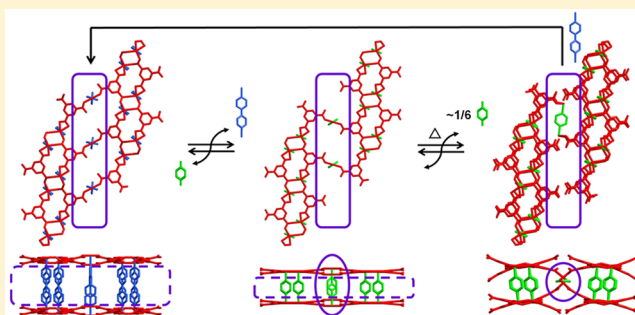
■ INTRODUCTION

Metal−organic frameworks (MOFs) are extended networks of metal ions (or clusters) and organic linkers as building blocks. Although there is significant progress in the design and prediction for the preparation of a new MOF,[1−7] it is still difficult to synthesize a MOF with the desired physical and chemical properties using *de novo* solvothermal reactions. A postsynthetic modification is an alternative approach to prepare a new MOF by modulating the building blocks of a MOF prepared using a *de novo* solvothermal reaction.[8−10] Both the postsynthetic covalent modification of an organic linker[11−24] and the postsynthetic dative modification of a metal coordination environment[25−28] in a MOF are very efficient ways to introduce a new functionality into the pore of the MOF, where the framework itself is not altered during the modification.

The framework can be altered either by exchanging the building blocks of a MOF[29−59] or by inserting new building blocks into a MOF.[60−63] When a framework metal ion is exchanged by a different metal ion with the same or a similar coordination property, an isostructural framework can be obtained in a single-crystal-to-single-crystal (SCSC) fashion with no significant structural reorganization.[29−46] When an organic linker of a MOF is exchanged by a different organic linker of the same or similar length, an isostructural framework can also be generated with no significant structural reorganization, as in the case of framework metal ion exchange.[47−59] In

contrast, the exchange of an organic linker using another organic linker of a different length can lead to an isoreticular MOF with a significant reorganization of the framework structure.[64−70] The most successful postsynthetic exchanges of the organic linkers that accompany one-dimensional (1-D) structural reorganization occurred in three-periodic (3-P) MOFs based on pillared sheets as two-periodic (2-P) supermolecular building blocks (SBBs). During the exchange of the pillaring linker, the 2-P SBB remains unaltered.[64−69] The ligand exchange that results in the three-dimensional (3-D) reorganization of the framework structure is reported in a 3-P framework based on a metal−organic polyhedron as zero-periodic (0-P) SBB, where the 0-P SBBs are triply connected to the other SBBs. The multiple connectivity between the 0-P SBBs allows even 3-D reorganization of the framework structure in an SCSC fashion.[70] However, a postsynthetic exchange of the organic linker that accompanies the two-dimensional (2-D) reorganization of the framework structure has not been reported.

Here, we present a postsynthetic exchange of the organic linker that involves an unprecedented 2-D reorganization of the 3-P framework structure, where the framework consists of a one-periodic (1-P) chain as an SBB, and the SBBs are interconnected to form the 3-P framework using both neutral
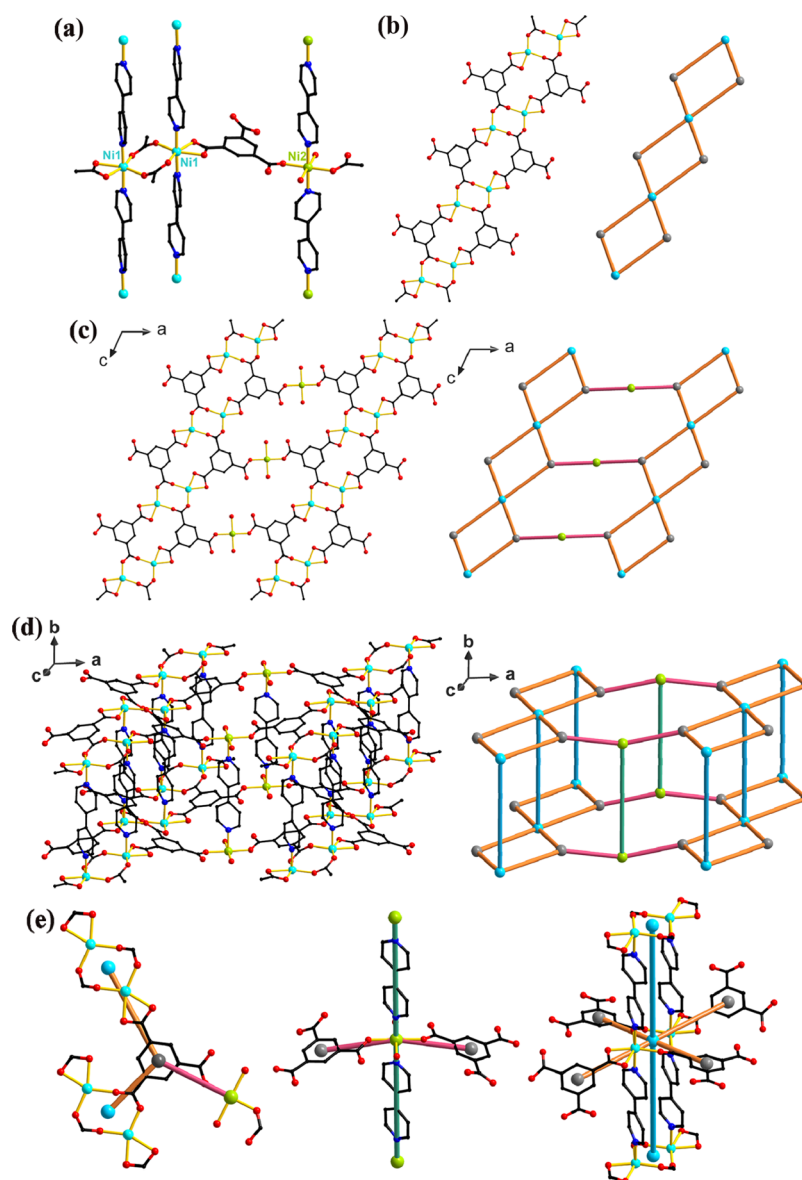
Figure 1. Crystal structure of **1**. (a) The coordination environments of the Ni^{II} ions and the ligands in **1**. (b) A ball-and-stick model of a 1-P *rhomboidal chain* structure and the corresponding node-and-linker diagram. (c) A ball-and-stick model of a 2-P sheet structure and the corresponding node-and-linker diagram. (d) A ball-and-stick model of a 3-P pillared structure and the corresponding node-and-linker diagram. (e) A 3-c node based on the btc ligand, a 4-c node based on the mononuclear Ni center, and a 6-c node based on the dinuclear $[Ni_2(COO)_4(N_2)_2]$ SBU.

diptotic organic linkers and ditopic metal ions. The neutral diptotic organic linker of the 3-P MOF can be replaced by another neutral diptotic organic linker in an SCSC fashion while keeping the 1-P chains as a stable SBB and unaltered during the transformation. The subsequent reversible deletion and insertion of the neutral organic linker and the reversible exchange of the neutral organic linkers are also observed.

■ **EXPERIMENTAL SECTION**

Preparation of MOFs. *Preparation of the MOF, [Ni₃(btc)₂(bipy)₃(H₂O)₂]·xDMF (1) (Where x is a Number of DMF Molecules in the Solvent Pore Per Formula Unit), Using a de Novo Solvothermal Reaction.* A solid mixture of $Ni(NO_3)_2 \cdot 6H_2O$ (0.0850 g, 0.292 mmol), 1,3,5-benzenetricarboxylic acid (H_3btc, 0.0522 g, 0.248 mmol), and 4,4′-bipyridine (bipy, 0.0526 g, 0.337 mmol) was dissolved in 48 mL of a *N,N*-dimethylformamide (DMF)/MeOH (3:1 ratio) mixed solvent in a 50 mL glass vial. The solution was divided into five portions, and each aliquot was heated to 120 °C in a flame-sealed glass tube for 7 days to form dark cyan crystals. The collected crystals were

washed with DMF and then air-dried in ambient conditions for 1 h. Infrared (IR) spectrum of **1** (KBr, cm⁻¹): 3392 (vs, b), 3066 (w, b), 2932(m, sh), 1667 (vs), 1634 (s), 1610 (vs), 1558 (s, sh), 1543 (s), 1491 (m), 1433 (s), 1415 (s), 1370 (vs), 1255 (w), 1222 (m), 1101 (m), 1070 (m), 1047 (w), 1012 (w), 939 (w), 860 (w), 817 (m), 770 (m), 729 (m, sh), 718 (m), 662 (w), 636 (m), 573 (w). The activated sample **1a** was prepared by soaking the crystals of **1** in fresh DMF for 3−4 days and in methylene chloride (MC) for an additional 2 days, and then vacuum-drying the crystals at 50 °C overnight. Elemental analysis (EA) was performed using the activated sample re-exposed in air for a couple of minutes before the analysis. EA calc. for $[Ni_3(btc)_2(bipy)_3(H_2O)_2] \cdot 18H_2O$ ($C_{48}H_{60}N_6O_{30}Ni_3$, fw = 1377.10 g/mol). Found (Calc.): C = 41.56 (41.87) %; H = 4.13 (4.39) %; N = 6.56 (6.10) %.

Preparation of the MOF, [Ni₃(btc)₂(pz)₃(H₂O)₂] (2), by a Postsynthetic Ligand Exchange of 1. A 50−100 mg amount of the crystals of **1** soaked in DMF was transferred into 10 mL of a 0.5 M pyrazine (pz) DMF solution in a 20 mL vial, and the vial was kept in an oven at 100 °C for 1−2 weeks, depending on the sample amount.

The solution was refreshed 2−3 times during the soaking. The progress of the ligand exchange was monitored using powder X-ray diffraction (PXRD). When the ligand exchange was completed, the greenish cyan crystals were harvested and washed more than three times using fresh DMF, and then air-dried at ambient temperature for 1 h. IR spectrum of **2** (KBr, cm^{-1}): 3380 (vs, b), 3116 (m), 3068 (m), 2956 (w), 2932 (w), 2850 (w), 1679 (vs), 1640 (vs), 1611 (m), 1555 (m), 1534 (s), 1487 (w), 1464 (w), 1436 (m), 1418 (m, sh), 1385 (m), 1373 (m), 1257 (w), 1218 (vw), 1162 (w), 1115 (w), 1098 (m), 1062 (m), 1032 (vw), 980 (vw), 941 (w), 819 (m), 769 (s), 733 (s), 718 (s), 662 (m), 571 (w), 524 (w), 482 (m), 453 (w), 430 (vw). The activated sample **2a** was prepared by soaking the crystals of **2** in fresh DMF for 3−4 days and in MC for an additional 2 days, and then vacuum-drying at room temperature for 1 day. EA was performed using the sample of **2a** re-exposed in air for several minutes before the analysis. EA calc. for $[Ni_3(btc)_2(pz)_3(H_2O)_2] \cdot 15H_2O$ ($C_{30}H_{42}N_6O_{27}Ni_3$, fw = 1094.76 g/mol). Found (Calc.): C = 32.89 (32.91) %; H = 3.45 (3.87) %; N = 7.75 (7.68) %.

Preparation of the MOF, $[Ni_6(btc)_4(pz)_{4.75}(H_2O)_5] \cdot 19H_2O$ (3), by a Postsynthetic Ligand Deletion of 2. Method A. When the pale bluish-green crystals of **2** (50−100 mg) were heated to 200 °C at a 10 °C/min heating rate, maintained for 1 h, and cooled to ambient temperature under flowing N_2, the crystals turned brown. When the brown crystals were exposed in air, they changed to the cyan crystals of **3** within several minutes (Figure S1). Method B. **3** can be alternatively prepared by vacuum-drying **2**, presoaked for 2 days in MC, at 200 °C for 1 h, and then exposed to air for 2−3 min. IR of **3** (KBr, cm^{-1}): 3354 (vs, b), 3120 (m), 3072 (m), 1683 (w), 1652 (m), 1634 (vs), 1621 (m), 1615 (m),1574 (w), 1568 (w), 1558 (s), 1538 (m), 1532 (w), 1506 (w), 1435 (s), 1423 (m), 1373 (vs), 1162 (w), 1120 (m), 1088 (vw), 1064 (m), 939 (vw), 817 (vw), 769 (s), 733 (s), 719 (m), 560 (w), 483 (m), 451 (w), 440 (vw). EA calc. for **3**, $[Ni_6(btc)_4(pz)_{4.75}(H_2O)_5] \cdot 19H_2O$ ($C_{55}H_{67}N_{9.5}O_{48}Ni_6$, fw = 1981.31 g/mol). Found (Calc.): C = 33.34 (31.82) %; H = 3.41 (3.25) %; N = 6.72 (6.96) %.

Reverse Transformations of the MOFs by a Postsynthetic Insertion and Exchange of the Ligand. *Reverse Transformation of 3 to 2 by a Postsynthetic Ligand Insertion.* A 50−100 mg amount of **3** crystals was soaked in a 10 mL 0.5 M pz DMF solution in a 20 mL vial and maintained at ambient conditions for 3−5 days, depending on the sample amount. When the transformation process was completed, the crystals were washed several times using fresh DMF, and then air-dried for 1 h.

Reverse Transformation of 2 to 1 by a Postsynthetic Ligand Exchange. A 50−100 mg amount of **2** crystals was immersed to 10 mL of a 0.5 M bipy DMF solution in a vial and kept at 100 °C for 1−2 weeks, depending on the sample amount. The solution was exchanged 2−3 times during the soaking period, and the progress of the ligand exchange was monitored by PXRD. When the ligand exchange was complete, the crystals were harvested and washed using fresh DMF more than three times, and then air-dried at ambient temperature for 1 h.

Reverse Transformation of 3 to 1 by a Postsynthetic Ligand Insertion and Exchange. A 50−100 mg amount of **3** crystals was soaked in 10 mL of a 0.5 M bipy DMF solution in a vial and kept at 100 °C for 1−2 weeks, depending on the sample amount. The solution was exchanged 2−3 times during the soaking period. When the transformation process was complete, the crystals were harvested and washed using fresh DMF several times, and then air-dried at ambient conditions for 1 h.

■ RESULTS AND DISCUSSION

***De Novo* Synthesis of 1 and Its Single Crystal Structure.** The microporous 3-P MOF **1** with the mixed ligands was obtained by a simple one-pot solvothermal reaction. The reaction of $Ni(NO_3)_2 \cdot 6H_2O$ as a source for potential metal-based nodes with two different types of ligands, btc as an anionic tritopic node, and bipy as a neutral ditopic linker, in a DMF/MeOH mixed solvent at 120 °C for 7 days led to the

formation of dark cyan crystals, $[Ni_3(btc)_2(bipy)_3(H_2O)_2]$ (**1**). The single-crystal X-ray structural analysis of **1** reveals that the two N^{II} ions (Ni1 and Ni2) in different coordination environments adopt the same *trans*-$[N_2O_4]$ octahedral geometry (Figure 1a). For Ni1, the equatorial plane of the octahedron is defined by four oxygen atoms from three carboxylates of btc ligands, and the axial positions are occupied by two nitrogen atoms from bipy ligands. Ni2 is ligated by two monodentate carboxylates, two nitrogen atoms from bipy ligands, and two water molecules. Ni1 is bridged by carboxylates in a bis(*syn-syn*) binding mode to form a dinuclear nickel cluster, $[Ni_2(COO)_4(N_2)_2]$, as a secondary building unit (SBU). The SBUs are doubly linked using two btc ligands to form a 1-P *rhomboidal chain* structure (Figure 1b). The 1-P *rhomboidal chains* are further connected by mononuclear Ni2 centers to form a 2-P sheet with a (3,4)-c **bex** topology (Figure 1c).[71] The 2-P sheets are pillared by bipy linkers to form a 3-P network (Figure 1d), where two different types of bipy pillarings are observed. The first type of pillaring is through the dinuclear nickel clusters. The dinuclear nickel clusters are doubly connected to the dinuclear nickel clusters of the adjacent 2-P sheets. The second type of pillaring is through the mononuclear nickel centers (Ni2) that interconnect the 1-P *rhomboidal chains* to form the 2-P sheet. The 3-P network **1** is a rare (3,4,6)-c net of sqc130 topology[72] consisting of the btc ligand as a 3-c node, the mononuclear Ni center as a 4-c node, and the dinuclear nickel cluster as a 6-c node (Figure 1e).

1 contains orthorhombic cage-like pores (cage dimension of 6.2 × 7.9 × 10.0 Å^3) that are interlinked by several different kinds of narrow portals to form a 3-D porous structure (Figure S2). The potential pore volume of **1** calculated using the SOLV option of PLATON[73] corresponds to 1670 Å^3 per unit cell, which is 44.2% of the total unit cell volume.

The bulk identity of the sample was checked by a comparison of the observed PXRD pattern of the as-synthesized **1** and the simulated PXRD pattern of the single-crystal structure model of **1** (Figure S3). The PXRD pattern of the as-synthesized **1** exposed at ambient conditions for approximately 10 min is not the same as the simulated pattern of **1**. Even a small amount of the guest solvent loss in the pore leads to a slight distortion of the framework. The sample, presoaked in MC and exposed to ambient conditions for approximately 10 min, showed a significant loss of crystallinity. However, the crystallinity of the sample could be restored by simply soaking the amorphous sample in DMF. The PXRD pattern of the restored sample is the same as that of as-synthesized **1**. The ^1H nuclear magnetic resonance (NMR) spectrum of as-synthesized **1** digested in a DCl/dimethyl sulfoxide-d_6 solution also indicates that the ratio of tritopic btc ligands and ditopic bipy linkers in the bulk sample is the same as that in the single crystal structure (Figure S4).

Preparation of the Isoreticular MOF, 2, by Postsynthetic Ligand Exchange of a Single-Crystal-to-Single-Crystal Transformation. *Preparation of the Isoreticular MOF, 2.* The 3-P MOF with the ditopic bipy pillars, $[Ni_3(btc)_2(bipy)_3(H_2O)_2]$ (**1**), could be transformed to another isoreticular MOF with ditopic pz pillars, $[Ni_3(btc)_2(pz)_3(H_2O)_2]$ (**2**), by pillar exchange. A simple soaking of **1** in a pz DMF solution at 100 °C led to pillar exchange. The dark cyan crystals of **1** turned to greenish cyan crystals of **2** (Figure S6). The complete exchange of the pillaring ligands was confirmed by ^1H NMR spectroscopy. The ^1H NMR spectrum of activated **2a** digested in a DCl/D$_2$O

solution showed that the bipy pillars are completely removed, and the btc ligands and the pz pillars are present in a stoichiometric ratio (Figure S7).

SCSC Transformation. To confirm whether the transformation from **1** to **2** by the postsynthetic exchange of the pillaring ligand is a SCSC transformation, one single crystal of **1** was soaked in a pz DMF solution for 1 day at 100 °C as for the bulk transformation. There is no indication of either the dissolution of the single crystal or the formation of new single crystals during the soaking. One single crystal remained during the whole transformation process, but its dimension was reduced (Figure 2). One dimension of the crystal is ~30%
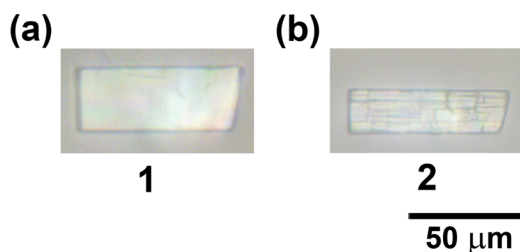
Figure 2. Optical microscopic photographs of a single crystal of **1** (a) before and (b) after soaking in a pz DMF solution for 1 day at 100 °C.

smaller after the soaking than the corresponding dimension of the crystal before the soaking, while keeping the other dimensions of the crystal unchanged.

Single Crystal Structure of 2. Though the space group of **2**, $P2/c$, is the same as that of **1**, the lattice parameters of **2** are significantly different from those of **1**. The replacement of the

bipy pillars, aligned along the crystallographic *b*-axis in **1**, with pz pillars leads to a significant reduction of the *b*-axis parameter in **2** (from 11.259(2) Å to 6.941(1) Å). Other noticeable differences are also observed for the β angles together with the *a*- and *c*-axis parameters, which imply that the pillar exchange affects not only the pillaring distance but also the 2-P sheet structure itself (Figure 1c). The single crystal structure analysis of **2** confirmed the complete replacement of the pillaring ligands. Even though the net topology of **2** is the same as that of **1**, the connectivity of **2** is not the same as that of **1** (Figure 3). During the pillaring ligand replacement, the interconnection between the 1-P *rhomboidal chains* in the 2-P sheet was also simultaneously changed. The relative interconnection between the 1-P *rhomboidal chains* in **2** is different from that in **1**. The linkages between carboxylate pairs (dashed pale pink sticks) in **1**, by mononuclear Ni2 centers interconnecting the adjacent 1-P *rhomboidal chains* to form the 2-P sheet, has shifted to the linkages of the other carboxylate pairs (solid purple sticks) in **2** (Figure 3a), which leads to a slight distortion of the 2-P sheet structure in the crystallographic *ac*-plane.

2 also contains orthorhombic cage-like pores with dimensions of 5.8 × 3.5 × 9.7 Å³, which are interlinked by several different kinds of narrow portals to form a 3-D porous structure as the orthorhombic cage-like pores of **1** (Figure S8). The reduction of the orthorhombic pore dimension in **2** compared to that in **1** comes mainly from the replacement of bipy pillars by short pz pillars. The potential pore volume of **2**, 1127 Å³ per unit cell, is also significantly reduced compared to that of **1**, 1670 Å³ per unit cell.

Bulk Identity and Stability of 2. The bulk identity of **2** was also verified by the comparison of the observed and simulated
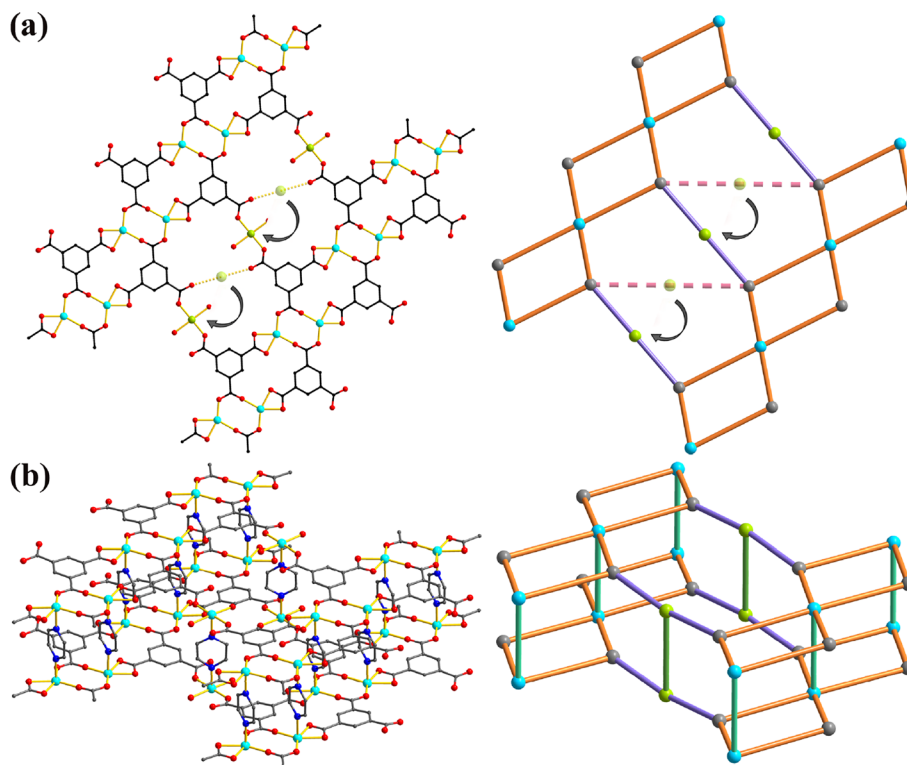

Figure 3. Crystal structure of **2**. (a) A ball-and-stick model of a 2-P sheet structure formed with 1-P *rhomboidal chains* connected by mononuclear Ni centers, and the corresponding node-and-linker diagram. The dashed pink sticks represent the old connectivity between carboxylate pairs of 1-P *rhomboidal chains* in **1**, and the solid purple sticks represent the new connectivity between the other carboxylate pairs of 1-P *rhomboidal chains* in **2**. (b) A ball-and-stick model of a 3-P pillared structure and the corresponding node-and-linker diagram.

PXRD patterns (Figure S9). The observed PXRD pattern of as-synthesized **2** matches well with the simulated pattern from the single crystal structure model. Activated **2a** is still crystalline and its PXRD pattern is very similar to that of as-synthesized **2**. The slight shifts of most peaks to higher diffraction angles indicate that the structure is quite rigid; however, there is a small amount of shrinkage of the overall framework when the solvent molecules are removed from the pore.

Thermal Properties of 2. The thermal properties of **2** were evaluated using thermogravimetric analysis (TGA). The analysis was performed using **2** presoaked in MC. The TGA profile indicates at least a six-step weight loss (Figure S10). The first two-step weight loss up to 150 °C (15.2 wt %) corresponds to the loss of 1.5 MC molecules (calcd. 12.7 wt %) and 1.5 H_2O molecules (calcd. 2.5 wt %) in the pore. The next two-step weight loss from 150 to 380 °C corresponds to some pz pillars and water molecules. The weight loss from 150 to 270 °C (4.5 wt %) is the loss of a 0.6 pz pillar (calcd. 4.7 wt %). The amount of pz pillar loss during the heating process up to 270 °C was confirmed by the ^1H NMR spectrum of the sample prepared by the same manner used for the TGA heating process. The weight loss from 270 to 300 °C (17.7 wt %) matches with the loss of two coordinated water molecules (calcd. 3.5 wt %) and 1.8 pz pillars (calcd. 14.2 wt %). Even though the boiling point of pz is higher than that of water, the loss of some pz linkers prior to that of the ligated water molecules is due to the intramolecular hydrogen-bond interaction of the water molecules with the carboxylate oxygens of the btc ligands (Figure S11). The final two-step weight loss that starts at 380 °C corresponds to the thermal decomposition of the remaining structure together with the loss of the remaining 0.6 pz pillar.

Preparation of the New MOF, 3, by Postsynthetic Deletion of Ligand. *PXRD Patterns of Heat-Treated 2.* Heat-treated samples were prepared using **2** crystals presoaked in MC. The crystals were heated to a given temperature at a rate of 10 °C min^{-1} and maintained for 1 h under flowing N_2. After being cooled to ambient temperature, the crystals were exposed in air before the PXRD measurement. **2** is stable up to 150 °C. The PXRD pattern of the heat-treated **2** up to 150 °C did not show any indications of the loss of crystallinity (Figure 4). A set of new diffraction peaks appeared at 180 °C together with the diffraction peaks from **2**. The diffraction peaks corresponding to **2** completely disappeared at 200 °C, and only the set of new diffraction peaks was observed. The new crystalline phase is stable at 220 °C but starts to lose its crystallinity at higher temperatures.

Ligand Compositions of the Heat-Treated 2 Samples. The ligand compositions of the heat-treated **2** samples were analyzed using the ^1H NMR spectra of the samples digested in a DCl/D_2O-d_6 solution (Figure S12). The number of pz linkers per btc ligand is temperature dependent, and it shows stepwise losses of pz linkers (Figure S13). The amount of pz linker loss up to the first step at 200 °C corresponds to one-sixth of the total pz linkers in the framework. The second stepwise loss up to 330 °C is two-thirds of the total pz linkers. Even though the two different types of pz linkers are present in a 2:1 ratio in the framework of **2**, the loss of one-sixth of the total pz linkers and the crystallinity of the heat-treated sample up to 200 °C indicates the possibility of the preparation of a new MOF with the pz linkers partially, but systematically, removed from the framework of **2**.
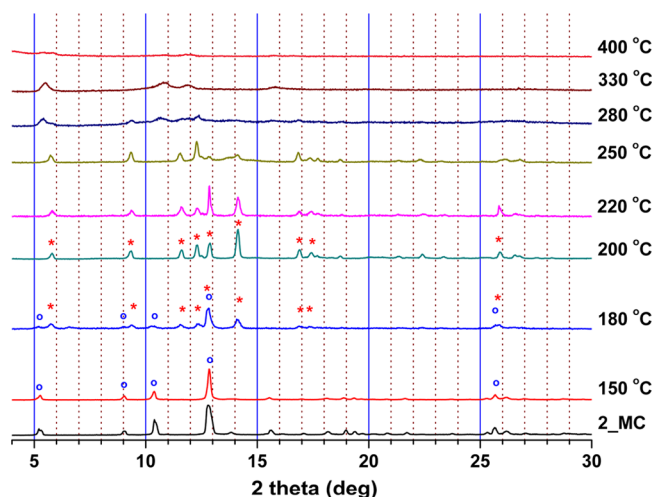

Figure 4. PXRD patterns of heat-treated **2** crystals presoaked in MC. The blue circles represent one set of the diffraction peaks from **2**, and the red asterisks represent another set of diffraction peaks from the heat-treated **2**.

Preparation of 3. Single crystals of **3** were obtained by heating single crystals of **2** at 200 °C for 1 h under flowing N_2, cooling to ambient temperature, and then exposing the crystals in air (Figure S14). The EA and the ratio of the btc ligand and pz pillar from the ^1H NMR spectrum of **3** indicate that the generated formula unit of **3** is $[Ni_6(btc)_4(pz)_{4.75}(H_2O)_5]\cdot 19H_2O$.

Crystal Structure of 3. A single crystal structure analysis revealed that the lattice parameters of **3** were completely different from those of **2**. The space group of **2**, $P2/c$, has changed to $C2/m$ in **3**, and the framework structure of **3** is also completely different from that of **2** (Figures 5 and S15). **2** with a (3,4,6)-c sqc130 net topology changed to **3** with an unprecedented (3,6)-c net topology of a $(4.5^2)_2(5.10^2)$-$(4^2.5^4.6^4.8.9^4)$ point symbol consisting of a btc ligand as a 3-c node, the mononuclear Ni center as a 3-c node, and the dinuclear nickel cluster as a 6-c node.[72] Approximately half of the pz pillars interconnecting the mononuclear Ni2 centers along the crystallographic b-axis in **2** (Figure 3b), which are one-sixth of the total pz linkers, are alternatively removed from **3** (Figures 5 and 6). The remaining pz pillars interconnecting the mononuclear Ni2 centers lay along the crystallographic c-axis. Each new Ni center interconnected by the remaining pz linker is further connected by two carboxylates of two different btc ligands, as shown in Figures 5a-b. The *trans*-coordination mode of two carboxylates in the mononuclear Ni center in **2** changed to the *cis*-coordination mode in the octahedral Ni center of the new dinuclear Ni cluster in **3** (Figure S16). Though the connectivity of the other parts of the structure itself does not change during the SCSC transformation from the *trans*-coordination mode to the *cis*-coordination mode in the octahedral Ni center, the geometry of the other parts of the structure in **3** is slightly twisted from that in **2**. The octahedral Ni ion in the new dinuclear cluster has 0.75 site occupancy and the other distorted tetrahedral Ni ion has 0.25 site occupancy. The new dinuclear Ni cluster in the crystal structure of **3** is the statistically disordered structure of the dinuclear Ni cluster of 0.25 site occupancy and of the mononuclear center of 0.50 site occupancy.

3 has spherical cage-like pores (~6 Å in diameter, Figure S17). The spherical pores are interlinked to form a complicated
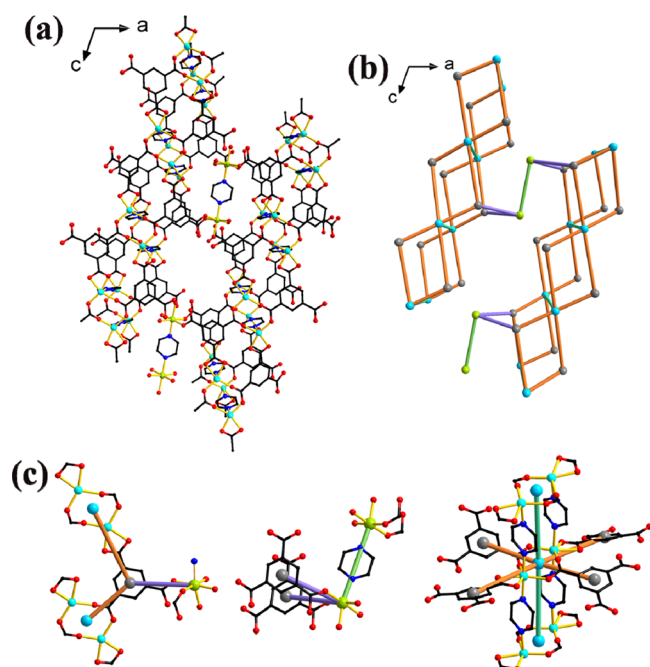
Figure 5. Crystal structure of **3**. (a) The projection view of **3** in a ball-and-stick model along the crystallographic *c*-axis. (b) The same projection view of the network of **3** in a node-and-linker diagram. (c) A 3-c node based on the btc ligand, a 3-c node based on the mononuclear Ni center, and a 6-c node based on the dinuclear $[Ni_2(COO)_4(N_2)_2]$ SBU.
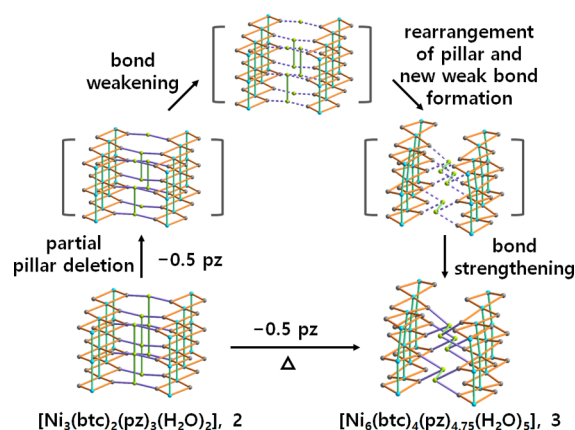
Figure 6. A proposed transformation process from **2** to **3**.

3-D porous structure by several different narrow portals with dimensions ranging up to 3.2 × 4.4 Å^2.
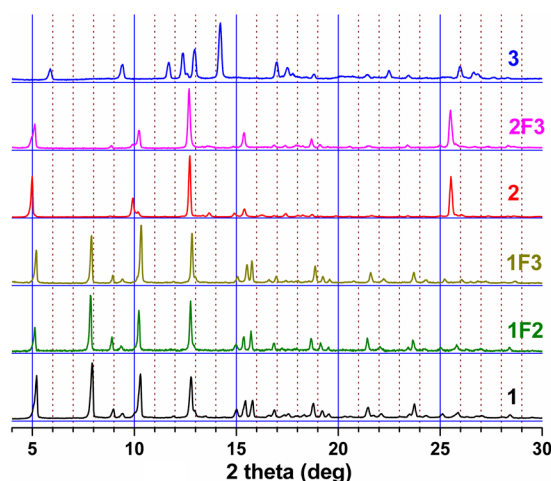
Transformations of the MOFs. *Transformations of the MOFs by a Ligand Exchange and Deletion.* **1** has a 3-P (3,4,6)-c sqc130 topology that contains bipy as a pillaring ligand between the 2-P sheet of a (3,4)-c **bex** topology and could be transformed to the isoreticular MOF **2** with pz as a pillaring ligand (Figure 7). During the transformation from **1** to **2**, the structural rearrangement occurs in two different ways, both between the 2-P sheets of the **bex** topology and within the sheet. The first structural rearrangement is between the sheets. The intersheet distance is reduced by the pillar exchange. The second structural rearrangement is within the 2-P sheet. The interlinkage between the 1-P *rhomboidal chains* in the 2-P sheet in **1** changes to a different interlinkage between the 1-P *rhomboidal chains* in the 2-P sheet in **2**. A set of the pairings
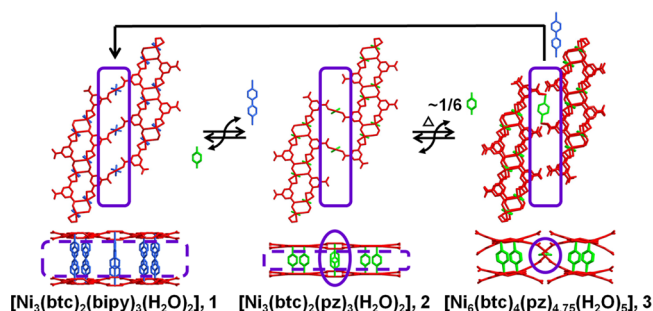
Figure 7. A scheme of reversible SCSC transformations by ligand exchange, deletion, and insertion.

between the two carboxylates in *trans*-binding mode in the mononuclear Ni2 center in **1** shifts to another set of the different pairings between the two different carboxylates in *trans*-binding mode in the mononuclear Ni2 center in **2**. **2** could be further transformed to **3** by deletion of some pillaring pz ligands. The controlled heating of **2** leads to partial, but systematic, removal of the pillaring ligands between the mononuclear Ni centers and the subsequent rearrangement of the remaining pillaring ligands between the mononuclear Ni centers along the 2-P sheet.

Reverse Transformations of the MOFs by a Ligand Insertion and Exchange. **3** can be transformed back to **2** by pz linker insertion (Figure 7). A simple soaking of **3** in a pz DMF solution at ambient conditions produces **2**. The PXRD pattern of **2F3** (where **nFm** is the MOF **n** obtained from the MOF **m**) is the same as that of as-synthesized **2** (Figure 8). **2**


Figure 8. PXRD patterns of **1F2**, **1F3**, and **2F3** obtained by a reverse transformation of **2** and **3**.

can also be transformed back to **1** by pillar exchange. Soaking **2** in a bipy DMF solution at 100 °C leads to **1** by isoreticular replacement of all pz pillars to bipy pillars. The PXRD pattern of **1F2** is also the same as that of as-synthesized **1** obtained by the *de novo* solvothermal reaction. **3** with the pz linker can also be directly transformed back to **1** by simultaneous replacement and insertion of bipy. The PXRD pattern of **1F3** is again indistinguishable from that of as-synthesized **1**.

Sorption Behaviors of the MOFs. *Gas Sorption Behaviors of 1a.* Although the PXRD pattern of activated **1a** shows the loss of its crystallinity, it shows stepwise N$_2$ adsorption and hysteric desorption at 77 K (Figure 9a). The
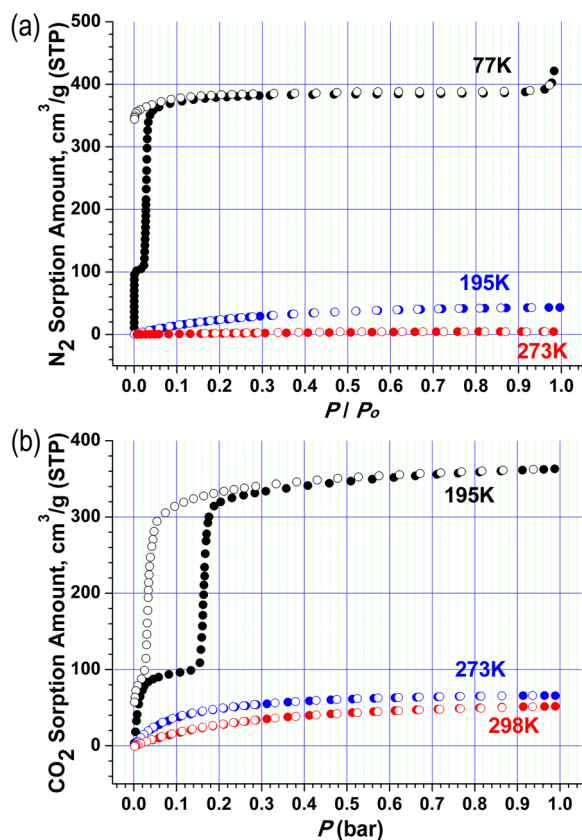
Figure 9. (a) N_2 sorption isotherms on **1a** at 77, 195, and 273 K. (b) CO_2 sorption isotherms on **1a** at 195, 273, and 298 K.

very steep N_2 adsorption reaches the first short plateau with ~100 cm³/g of uptake at ~0.01 P/P_0. The second uptake starts at 0.023 P/P_0 and reaches a total uptake of 392 cm³/g at 0.96 P/P_0. While the specific pore volume of **1a** that was estimated from the uptake amount of 100 cm³/g at 0.01 P/P_0 (0.155 cm³/g) is much smaller than the calculated specific pore volume of **1** from the single crystal structure (0.459 cm³/g), the specific pore volume of **1a** estimated from the uptake amount of 392 cm³/g at 0.96 P/P_0, 0.606 cm³/g, is even larger than the calculated specific pore volume. **1a**, with a partially collapsed pore, can be restored by N_2 at 77 K. The Brunauer−Emmett−Teller (BET) surface area of the partially collapsed **1a** was calculated as 470 m²/g using the adsorption isotherm data of P/P_0 between 0.0006 and 0.0229. The BET surface area of the restored **1a** calculated using the adsorption isotherm data of P/P_0 between 0.031 and 0.084 is 1510 m²/g, which is again slightly larger than the calculated BET surface area, 1260 m²/g, using the crystal structure model of **1**.[74] The hysteric desorption starts at the very low pressure, ~0.005P/P_0. There is only a negligible amount of N_2 adsorption at 273 K, which is probably due to the weak interaction of N_2 with the pore surface, even though **1a** has some N_2 accessible pores. The reversible N_2 sorptions on **1a** at 195 K confirm the presence of some N_2 accessible pores. There is no stepwise adsorption, and the maximum adsorption amount at 1 bar is only 43 cm³/g. The interaction of N_2 with the framework at 195 K is not strong enough for complete pore restoration.

The CO_2 sorption behavior on **1a** at 195 K is similar to the N_2 sorption behavior at 77 K (Figure 9b). The CO_2 adsorption is also stepwise. The first steep adsorption reaches a plateau of ~100 cm³/g uptake at ~0.1 bar. The second adsorption step

starts at ~0.16 bar and reaches a total uptake of 360 cm³/g at ~0.99 bar. The hysteric first desorption starts at ~0.1 bar, and the second desorption occurs at ~0.018 bar. In contrast, the CO_2 sorptions on **1a** at 273 and 298 K are different from that at 195 K. There is no hysteresis and no stepwise adsorptions. The maximum uptakes at 273 and 298 K are 66 and 52 cm³/g at 1.0 bar, respectively. The partially collapsed pore of **1a** was not restored by CO_2 adsorptions at both 273 and 298 K. The CO_2 interactions with the framework of **1a** at these temperatures were not strong enough for restoration of the partially collapsed pore. **1a** shows reversible CH_4 sorption at 195, 273, and 298 K, respectively, using its partially collapsed pore (Figure S18). However, the partially collapsed pore of **1a** was not restored by CH_4 adsorption, even at 195 K.

The N_2 sorption isotherms on **2a** and **3** at 77 K are typical type I isotherms (Figure S19). The pore volumes estimated from the maximum uptake amounts at the saturation pressure, 0.422 and 0.320 cm³/g, respectively, are approximately matched with the calculated values from the corresponding single crystal structures, 0.391 and 0.270 cm³/g,[75] respectively. The BET surface areas of **2a** and **3**, 1060 m²/g and 810 m²/g, respectively, were calculated using the adsorption isotherm data of P/P_0 between 0.005 and 0.031 and between 0.0001 and 0.034, respectively. The isoreticular exchange of the long pillaring ligand bipy in **1a** by short pillaring ligand pz in **2a** leads to the reduction of the pore volume and the surface area. The partial and systematic removal of the pz ligand in **2a** and the subsequent transformation of the framework structure to **3** further reduces the pore volume and the surface area.

The CO_2 sorption behavior on **2a** and **3** at 195 K are also similar to the corresponding N_2 sorption behaviors (Figure S20). The CO_2 sorption isotherms are typical reversible type I isotherms with no hysteresis. The maximum CO_2 uptake on **2a** and **3** at 1 bar is 247 and 193 cm³/g, respectively.

The CO_2 adsorption enthalpies of **1a**, **2a**, and **3** were calculated using the CO_2 adsorption isotherms at 273 and 298 K, respectively, using virial-type fits (Figure 10a).[76] **1a** has the largest CO_2 adsorption enthalpy, which ranges from 36.3 to 33.5 kJ/mol (Figure 10b). **1a** has a partially collapsed pore that can provide the most effective interaction with CO_2 because it has the smallest pore dimension. The CO_2 adsorption enthalpies of **2a** and **3** range from 31.2 to 28.9 kJ/mol and from 20.7 to 19.5 kJ/mol, respectively. Even though **2a** has a larger pore volume and surface area than **3**, the pore size analyses using nonlocalized density functional theory[77] indicate that the average pore dimension of **2a**, ~0.60 nm, is smaller than that of **3**, ~0.65 nm (Figure 10c). The smaller pore dimension of **2a** than **3** is responsible for the larger CO_2 adsorption enthalpy of **2a** than **3**.

■ CONCLUSIONS

1 was prepared using a *de novo* solvothermal reaction with three different kinds of building blocks: the Ni(II) ion as a potential dicationic multitopic node, btc ligand as a potential trianionic tritopic ligand, and bipy as a neutral ditopic linker. The network of **1**, with a rare (3,4,6)-c sqc130 topology, contains the btc ligand as a 3-c node, a mononuclear Ni center as 4-c node, a dinuclear nickel cluster $[Ni_2(COO)_4(N_2)_2]$ as a 6-c node, and bipy as a ditopic linker between the metal-based nodes. In **1**, the dinuclear nickel clusters are doubly linked by carboxylates of the btc ligands to form a 1-P *rhomboidal chain* as a SBB, and the SBBs are further connected to form a 3-P network using both the mononuclear Ni centers and the two different types of
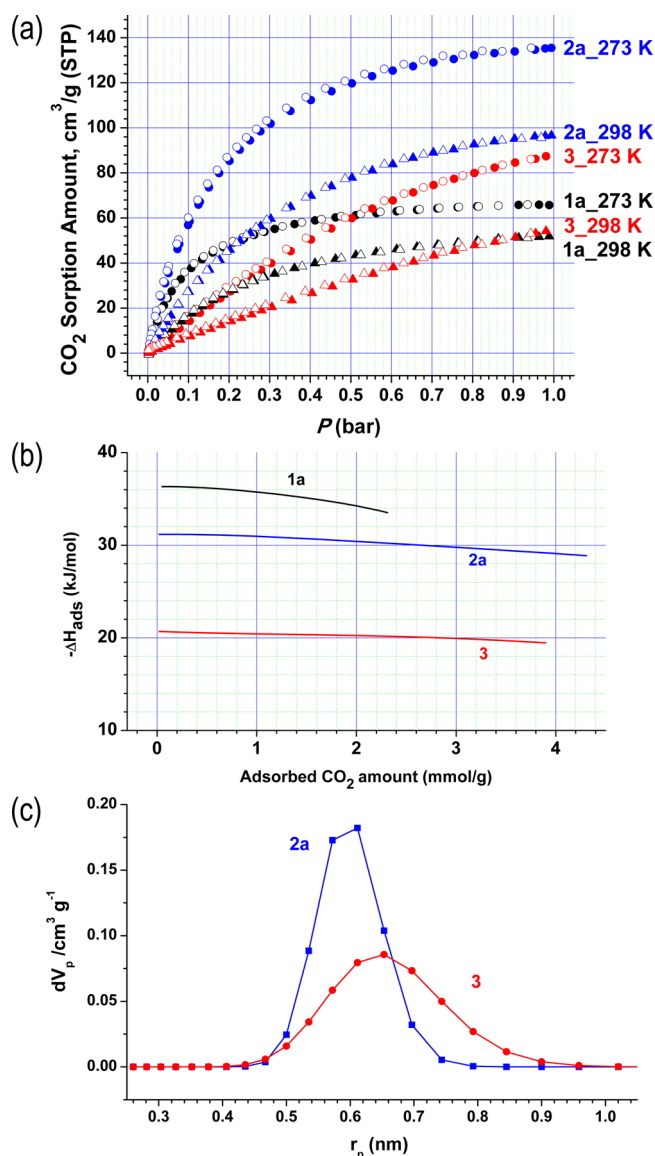
Figure 10. (a) CO_2 sorption behavior of **1a**, **2a**, and **3** at 273 and 298 K. (b) The adsorption enthalpy of **1a** (black), **2a** (blue), and **3** (red) calculated using virial-type fits. (c) Pore size distribution of **2a** and **3**.

bipy linkages. **1**, which contains 3-D solvent pores, loses its crystallinity when the pore solvent molecules are removed; however, it still shows reversible N_2 and CO_2 gas sorption behaviors with significant adsorption and desorption hysteresis. The stepwise adsorptions of N_2 and CO_2 are due to the flexibility of the framework.

1 can be transformed to **2** by a postsynthetic exchange of a neutral ditopic ligand. All the ditopic bipy linkers in **1** are replaced by similar but shorter ditopic pz linkers, which leads to an increase in the framework rigidity of **2** compared to that of **1**. The SCSC transformation from **1** to **2** accompanies the unprecedented 2-D structural reorganization during the exchange of the ligand. The major structural reorganization occurs along the neutral ditopic linker direction. The replacement from bipy to pz leads to the compressed stacking of the 2-P sheets of a **bex** topology. The other structural reorganization simultaneously occurred within the sheet. The pairings between the 1-P *rhomboidal chains* by the mononuclear Ni centers changed from one pairing between two close btc

ligands to the other pairing between the other two close btc ligands, as shown in Figure 3a. The stability of the 1-P *rhomboidal chain* structure as an SBB allowed the 2-D structural reorganization during the pillar exchange.

2 is much more stable than **1** because of the enhanced framework rigidity with short pz pillars. The enhanced framework rigidity and the presence of two different types of neutral ditopic pz pillars allow the partial but systematic removal of some pz linkers from the framework of **2**. Even though the coordination geometry of the bridging Ni center between the 1-P *rhomboidal chain* structures is significantly modified during the transformation from **2** to **3**, the single crystal crystallinity of the framework structure is maintained. In addition, the SCSC transformations can occur reversibly by postsynthetic insertion of the ligand and by postsynthetic exchange of the ligand. The stable 1-P SBB plays a pivotal role during the transformations that accompany significant 2-D reorganization of the framework structures.

■ ASSOCIATED CONTENT

ⓢ Supporting Information

The Supporting Information is available free of charge on the ACS Publications website at DOI: 10.1021/acs.cgd.7b00321.

> Optical microscopic photographs of **1**−**3**; crystal structure analyses of **1**−**3**; space-filling models of the cage-like pores of **1**−**3**; TGA data of **1** and **2**; PXRD data of **1**−**3**; ^1H NMR spectra of **1** and **2a**; crystal structure models of **3**; disordered dinuclear Ni cluster of **3**; CH_4 sorption isotherms on **1a**; N_2 sorption isotherms on **2a** and **3** at 77 K; CO_2 sorption isotherms on **2a** and **3** at 195 K (PDF)

Accession Codes

CCDC 1492769−1492771 contain the supplementary crystallographic data for this paper. These data can be obtained free of charge via www.ccdc.cam.ac.uk/data_request/cif, or by emailing data_request@ccdc.cam.ac.uk, or by contacting The Cambridge Crystallographic Data Centre, 12 Union Road, Cambridge CB2 1EZ, UK; fax: +44 1223 336033.

■ AUTHOR INFORMATION

Corresponding Author

*E-mail: mslah@unist.ac.kr.

Notes

The authors declare no competing financial interest.

■ ACKNOWLEDGMENTS

■ REFERENCES

(1) Yaghi, O. M.; O'Keeffe, M.; Ockwig, N. W.; Chae, H. K.; Eddaoudi, M.; Kim, J. *Nature* **2003**, *423*, 705−714.

(2) O'Keeffe, M.; Yaghi, O. M. *Chem. Rev.* **2012**, *112*, 675−702.

(3) Li, M.; Li, D.; O'Keeffe, M.; Yaghi, O. M. *Chem. Rev.* **2014**, *114*, 1343−1370.

(4) Lu, W.; Wei, Z.; Gu, Z.-Y.; Liu, T.-F.; Park, J.; Park, J.; Tian, J.; Zhang, M.; Zhang, Q.; Gentle, T., III; Bosch, M.; Zhou, H.-C. *Chem. Soc. Rev.* **2014**, *43*, 5561−5593.

(5) Guillerm, V.; Kim, D.; Eubank, J. F.; Luebke, R.; Liu, X.; Adil, K.; Lah, M. S.; Eddaoudi, M. *Chem. Soc. Rev.* **2014**, *43*, 6141−6172.

(6) Alexandrov, E. V.; Virovets, A. V.; Blatov, V. A.; Peresypkina, E. V. *Chem. Rev.* **2015**, *115*, 12286−12319.

(7) Cook, T. R.; Zheng, Y.-R.; Stang, P. J. *Chem. Rev.* **2013**, *113*, 734−777.

(8) Cohen, S. M. *Chem. Rev.* **2012**, *112*, 970−1000.

(9) Han, Y.; Li, J.-R.; Xie, Y.; Guo, G. *Chem. Soc. Rev.* **2014**, *43*, 5952−5981.

(10) Deria, P.; Mondloch, J. E.; Karagiaridi, O.; Bury, W.; Hupp, J. T.; Farha, O. K. *Chem. Soc. Rev.* **2014**, *43*, 5896−5912.

(11) Peikert, K.; Hoffmann, F.; Fröba, M. *Chem. Commun.* **2012**, *48*, 11196−11198.

(12) Allen, C. A.; Cohen, S. M. *J. Mater. Chem.* **2012**, *22*, 10188−10194.

(13) Sun, F.; Yin, Z.; Wang, Q.-Q.; Sun, D.; Zeng, M.-H.; Kurmoo, M. *Angew. Chem., Int. Ed.* **2013**, *52*, 4538−4543.

(14) Ishiwata, T.; Furukawa, Y.; Sugikawa, K.; Kokado, K.; Sada, K. *J. Am. Chem. Soc.* **2013**, *135*, 5427−5432.

(15) Tuci, G.; Rossin, A.; Xu, X.; Ranocchiari, M.; van Bokhoven, J. A.; Luconi, L.; Manet, I.; Melucci, M.; Giambastiani, G. *Chem. Mater.* **2013**, *25*, 2297−2308.

(16) Gross, A. F.; Sherman, E.; Mahoney, S. L.; Vajo, J. J. *J. Phys. Chem. A* **2013**, *117*, 3771−3776.

(17) Hintz, H.; Wuttke, S. *Chem. Commun.* **2014**, *50*, 11472−11475.

(18) Hintz, H.; Wuttke, S. *Chem. Mater.* **2014**, *26*, 6722−6728.

(19) Denny, M. S., Jr.; Cohen, S. M. *Angew. Chem., Int. Ed.* **2015**, *54*, 9029−9032.

(20) Wittmann, T.; Siegel, R.; Reimer, N.; Milius, W.; Stock, N.; Senker, J. *Chem. - Eur. J.* **2015**, *21*, 314−323.

(21) Dietl, C.; Hintz, H.; Rühle, B.; Schmedt auf der Günne, J.; Langhals, H.; Wuttke, S. *Chem. - Eur. J.* **2015**, *21*, 10714−10720.

(22) Bonnefoy, J.; Legrand, A.; Quadrelli, E. A.; Canivet, J.; Farrusseng, D. *J. Am. Chem. Soc.* **2015**, *137*, 9409−9416.

(23) Marshall, R. J.; Griffin, S. L.; Wilson, C.; Forgan, R. S. *J. Am. Chem. Soc.* **2015**, *137*, 9527−9530.

(24) Xi, F. G.; Liu, H.; Yang, N.-N.; Gao, E.-Q. *Inorg. Chem.* **2016**, *55*, 4701−4703.

(25) Bernini, M. C.; Gándara, F.; Iglesias, M.; Snejko, N.; Gutiérrez-Puebla, E.; Brusau, E. V.; Narda, G. E.; Monge, M. Á. *Chem. - Eur. J.* **2009**, *15*, 4896−4905.

(26) Deria, P.; Mondloch, J. E.; Tylianakis, E.; Ghosh, P.; Bury, W.; Snurr, R. Q.; Hupp, J. T.; Farha, O. K. *J. Am. Chem. Soc.* **2013**, *135*, 16801−16804.

(27) Deria, P.; Bury, W.; Hupp, J. T.; Farha, O. K. *Chem. Commun.* **2014**, *50*, 1965−1968.

(28) Chen, J.; Liu, R.; Gao, H.; Chen, L.; Ye, D. *J. Mater. Chem. A* **2014**, *2*, 7205−7213.

(29) Lalonde, M.; Bury, W.; Karagiaridi, O.; Brown, Z.; Hupp, J. T.; Farha, O. K. *J. Mater. Chem. A* **2013**, *1*, 5453−5468.

(30) Brozek, C. K.; Dincă, M. *Chem. Soc. Rev.* **2014**, *43*, 5456−5467.

(31) Wang, H.; Meng, W.; Wu, J.; Ding, J.; Hou, H.; Fan, Y. *Coord. Chem. Rev.* **2016**, *307*, 130−146.

(32) Dincă, M.; Long, J. R. *J. Am. Chem. Soc.* **2007**, *129*, 11172−11176.

(33) Das, S.; Kim, H.; Kim, K. *J. Am. Chem. Soc.* **2009**, *131*, 3814−3815.

(34) Song, X.; Kim, T. K.; Kim, H.; Kim, D.; Jeong, S.; Moon, H. R.; Lah, M. S. *Chem. Mater.* **2012**, *24*, 3065−3073.

(35) Song, X.; Jeong, S.; Kim, D.; Lah, M. S. *CrystEngComm* **2012**, *14*, 5753−5756.

(36) Kim, Y.; Das, S.; Bhattacharya, S.; Hong, S.; Kim, M. G.; Yoon, M.; Natarajan, S.; Kim, K. *Chem. - Eur. J.* **2012**, *18*, 16642−16648.

(37) Mukherjee, G.; Biradha, K. *Chem. Commun.* **2012**, *48*, 4293−4295.

(38) Brozek, C. K.; Dincă, M. *J. Am. Chem. Soc.* **2013**, *135*, 12886−12891.

(39) Lau, C. H.; Babarao, R.; Hill, M. R. *Chem. Commun.* **2013**, *49*, 3634−3636.

(40) Wang, X.-S.; Chrzanowski, M.; Wojtas, L.; Chen, Y.-S.; Ma, S. *Chem. - Eur. J.* **2013**, *19*, 3297−3301.

(41) Wei, Z.; Lu, W.; Jiang, H.-L.; Zhou, H.-C. *Inorg. Chem.* **2013**, *52*, 1164−1166.

(42) Yang, J.; Wang, X.; Dai, F.; Zhang, L.; Wang, R.; Sun, D. *Inorg. Chem.* **2014**, *53*, 10649−10653.

(43) Sen, S.; Neogi, S.; Rissanen, K.; Bharadwaj, P. K. *Chem. Commun.* **2015**, *51*, 3173−3176.

(44) Denysenko, D.; Jelic, J.; Reuter, K.; Volkmer, D. *Chem. - Eur. J.* **2015**, *21*, 8188−8199.

(45) Wang, X.; Zhang, L.; Yang, J.; Dai, F.; Wang, R.; Sun, D. *Chem. - Asian J.* **2015**, *10*, 1535−1540.

(46) Meng, W.; Li, H.; Xu, Z.; Du, S.; Li, Y.; Zhu, Y.; Han, Y.; Hou, H.; Fan, Y.; Tang, M. *Chem. - Eur. J.* **2014**, *20*, 2945−2952.

(47) Karagiaridi, O.; Bury, W.; Mondloch, J. E.; Hupp, J. T.; Farha, O. K. *Angew. Chem., Int. Ed.* **2014**, *53*, 4530−4540.

(48) Kim, M.; Cahill, J. F.; Su, Y.; Prather, K. A.; Cohen, S. M. *Chem. Sci.* **2012**, *3*, 126−130.

(49) Kim, M.; Cahill, J. F.; Fei, H.; Prather, K. A.; Cohen, S. M. *J. Am. Chem. Soc.* **2012**, *134*, 18082−18088.

(50) Karagiaridi, O.; Bury, W.; Sarjeant, A. A.; Stern, C. L.; Farha, O. K.; Hupp, J. T. *Chem. Sci.* **2012**, *3*, 3256−3260.

(51) Fei, H.; Cahill, J. F.; Prather, K. A.; Cohen, S. M. *Inorg. Chem.* **2013**, *52*, 4011−4016.

(52) Takaishi, S.; DeMarco, E. J.; Pellin, M. J.; Farha, O. K.; Hupp, J. T. *Chem. Sci.* **2013**, *4*, 1509−1513.

(53) Hong, D. H.; Suh, M. P. *Chem. - Eur. J.* **2014**, *20*, 426−434.

(54) Zhao, J.; Li, H.; Han, Y.; Li, R.; Ding, X.; Feng, X.; Wang, B. *J. Mater. Chem. A* **2015**, *3*, 12145−12148.

(55) Park, J.; Feng, D.; Zhou, H.-C. *J. Am. Chem. Soc.* **2015**, *137*, 1663−1672.

(56) Park, J.; Feng, D.; Zhou, H.-C. *J. Am. Chem. Soc.* **2015**, *137*, 11801−11809.

(57) Fei, H.; Cohen, S. M. *J. Am. Chem. Soc.* **2015**, *137*, 2191−2194.

(58) Liu, C.; Luo, T.-Y.; Feura, E. S.; Zhang, C.; Rosi, N. L. *J. Am. Chem. Soc.* **2015**, *137*, 10508−10511.

(59) Fei, H.; Pullen, S.; Wagner, A.; Ott, S.; Cohen, S. M. *Chem. Commun.* **2015**, *51*, 66−69.

(60) (a) Park, H. J.; Cheon, Y. E.; Suh, M. P. *Chem. - Eur. J.* **2010**, *16*, 11662−11669.

(61) Burnett, B. J.; Choe, W. *CrystEngComm* **2012**, *14*, 6129−6131.

(62) Yuan, S.; Lu, W.; Chen, Y.-P.; Zhang, Q.; Liu, T.-F.; Feng, D.; Wang, X.; Qin, J.; Zhou, H.-C. *J. Am. Chem. Soc.* **2015**, *137*, 3177−3180.

(63) Müller, P.; Wisser, F. M.; Bon, V.; Grünker, R.; Senkovska, I.; Kaskel, S. *Chem. Mater.* **2015**, *27*, 2460−2467.

(64) (a) Burnett, B. J.; Choe, W. *Dalton Trans.* **2012**, *41*, 3889−3894.

(65) Burnett, B. J.; Barron, P. M.; Hu, C.; Choe, W. *J. Am. Chem. Soc.* **2011**, *133*, 9984−9987.

(66) Karagiaridi, O.; Bury, W.; Tylianakis, E.; Sarjeant, A. A.; Hupp, J. T.; Farha, O. K. *Chem. Mater.* **2013**, *25*, 3499−3503.

(67) Jeong, S.; Kim, D.; Song, X.; Choi, M.; Park, N.; Lah, M. S. *Chem. Mater.* **2013**, *25*, 1047−1054.

(68) Bury, W.; Fairen-Jimenez, D.; Lalonde, M. B.; Snurr, R. Q.; Farha, O. K.; Hupp, J. T. *Chem. Mater.* **2013**, *25*, 739−744.

(69) Jeong, S.; Kim, D.; Shin, S.; Moon, D.; Cho, S. J.; Lah, M. S. *Chem. Mater.* **2014**, *26*, 1711−1719.

(70) Li, T.; Kozlowski, M. T.; Doud, E. A.; Blakely, M. N.; Rosi, N. L. *J. Am. Chem. Soc.* **2013**, *135*, 11688−11691.

(71) O'Keeffe, M.; Peskov, M. A.; Ramsden, S. J.; Yaghi, O. M. *Acc. Chem. Res.* **2008**, *41*, 1782−1789.

(72) TOPOS program: Blatov, V. A. *IUCr CompComm Newsletter* **2006**, *7*, 4−38.

(73) PLATON program: Spek, A. L. *Acta Crystallogr., Sect. D: Biol. Crystallogr.* **2009**, *65*, 148−155.

(74) Düren, T.; Millange, F.; Férey, G.; Walton, K. S.; Snurr, R. Q. *J. Phys. Chem. C* **2007**, *111*, 15350−15356.

(75) The calculated pore volume of **3** is the weight-averaged value obtained by using the three statistically disordered structure models of the new metal-based 3-c node shown in Figure S16.

(76) Rowsell, J. L. C.; Yaghi, O. M. *J. Am. Chem. Soc.* **2006**, *128*, 1304−1315.

(77) *BELMaster*, Ver. 6.1.0.8; BEL Japan, Inc.